Microdosimetry in low energy proton beam at therapeutic-equivalent fluence rate with silicon 3D-cylindrical microdetectors

To cite this article: C Guardiola *et al* 2021 *Phys. Med. Biol.* **66** 114001

View the article online for updates and enhancements.

Physics in Medicine & Biology

IPEM Institute of Physics and Engineering in Medicine

Microdosimetry in low energy proton beam at therapeutic-equivalent fluence rate with silicon 3D-cylindrical microdetectors

C Guardiola[1,2] , **D Bachiller-Perea**[1,2] , **J Prieto-Pena**[3], **M C Jiménez-Ramos**[4] , **J García López**[4,5] ,
C Esnault[1,2], **C Fleta**[6] , **D Quirion**[6] and **F Gómez**[3]

1 Université Paris-Saclay, CNRS/IN2P3, IJCLab, F-91405 Orsay, France
2 Université de Paris, IJCLab, F-91405 Orsay France
3 Departamento de Física de Partículas, Universidad de Santiago de Compostela, E-15782, Spain
4 Centro Nacional de Aceleradores, E-41092 Sevilla, Spain
5 Departamento de Física Atómica, Molecular y Nuclear, University of Sevilla, E-41080, Sevilla, Spain
6 Centro Nacional de Microelectrónica (IMB-CNM, CSIC), Bellaterra, E-08193, Spain

E-mail: consuelo.guardiola@ijclab.in2p3.fr

Keywords: microdosimetry, proton therapy, silicon 3D microdetectors

Abstract

In this work we show the first microdosimetry measurements on a low energy proton beam with therapeutic-equivalent fluence rates by using the second generation of 3D-cylindrical microdetectors. The sensors belong to an improved version of a novel silicon-based 3D-microdetector design with electrodes etched inside silicon, which were manufactured at the National Microelectronics Centre (IMB-CNM, CSIC) in Spain. A new microtechnology has been employed using quasi-toroid electrodes of 25 μm diameter and a depth of 20 μm within the silicon bulk, resulting in a well-defined cylindrical radiation sensitive volume. These detectors were tested at the 18 MeV proton beamline of the cyclotron at the National Accelerator Centre (CNA, Spain). They were assembled into an in-house low-noise readout electronics to assess their performance at a therapeutic-equivalent fluence rate. Microdosimetry spectra of lineal energy were recorded at several proton energies starting from 18 MeV by adding 50 μm thick tungsten foils gradually at the exit-window of the cyclotron external beamline, which corresponds to different depths along the Bragg curve. The experimental $\overline{y_F}$ values in silicon cover from (5.7 ± 0.9) to (8.5 ± 0.4) keV $\mu\mathrm{m}^{-1}$ in the entrance to (27.4 ± 2.3) keV $\mu\mathrm{m}^{-1}$ in the distal edge. Pulse height energy spectra were crosschecked with Monte Carlo simulations and an excellent agreement was obtained. This work demonstrates the capability of the second generation 3D-microdetectors to assess accurate microdosimetric distributions at fluence rates as high as those used in clinical centers in proton therapy.

1. Introduction

Proton therapy (PT) achieves very high dose conformity around the target, allowing a better protection of healthy surrounding organs at risk (Schardt D *et al* 2010). PT is included within the category of hadron beam therapy that allows the use of proton and heavier ions to improve the therapeutic index with respect to conventional photon radiotherapy (RT). Hadrons are more advantageous with respect to conventional RT mainly due to: (a) the physical depth-dose distribution that they deliver has a smaller dose in the entrance in tissue compared with conventional RT, but depositing a larger amount at the end of their ranges (Bragg peak) with a sharp fall-off at the distal edge; (b) the higher energy deposited in the center of their tracks generates a ionization density with a spatial distribution that produces a more complex cellular lesion that, in turn, may lead to non-reparable cellular damage along time (Paganetti 2010). This property is accounted for in terms of the relative biological effectiveness (RBE), which is defined as the ratio between the dose required to achieve a given biological effect with a reference beam quality, mostly 250 kV x-ray or ^{60}Co gamma rays, and that to achieve the same effect with other radiation quality (IAEA 2008). RBE value depends on the type of hadron and linear energy

transfer (LET), among other parameters, and it must be well characterized for correcting RT treatment plans. The higher the LET, the larger the hadron RBE. While in conventional RT the biological effect of radiation used is considered constant throughout the treatment volume, in higher-LET particle therapy the radiobiological effect depends strongly on the LET. For this reason, LET is a required input for the radiobiological optimization of hadron treatment plans. Therefore, to quantify the radiobiological effect, it is necessary to evaluate stochastic physical parameters such as the lineal energy (y), which is the microscopic quantity equivalent to the macroscopic LET. An under/overestimation of the real RBE could lead to induced toxicity in normal tissues or deliver an underdose of the target respectively. The calculation of biological dose distributions with RBE needs the characterization of the beam quality by means of the lineal energy distributions with precise microdosimeters of high spatial resolution, as the proposed herein. It must also include the corresponding radio sensibilities of the irradiated tissues. The microdosimetry data can be implemented in the well-established models that are currently used for clinical treatments, e.g. the local effect model (LEM) or microdosimetric-kinetic model (MKM) (Kase *et al* 2008), to calculate the associated RBE. Then, both physical and biological optimization can be carried out (i) removing high-LET spots from critical structures, (ii) focalizing high-LET regions into the target, and (iii) assessing the potential biological impact of the proton treatment plan on the target and surrounding normal tissue. It would allow us to guide beam arrangements to enhance therapeutic ratios and minimize dose excesses due to physical uncertainties. In particular, clinical implementation of RBE mitigations in the distal edge requires LET-based optimization. It can be performed by using LET-painting (Niels Bassler *et al* 2010), i.e. redistributing the LET by treatment plan optimization and maximizing LET in the target volume. LET-painting has demonstrated an increase of the tumor control probability in hypoxic tumors (Niels Bassler *et al* 2014). Likewise, Guan *et al* (2018) have recently proposed a biological effect model based on the dose-averaged LET into dose optimization algorithms for scanned protons. In this line, Gutierrez *et al* (2019) have evaluated the impact of LET/RBE modeling on base-of-skull and paediatric proton plans, showing that variable RBE-weighted doses predicted more hotspots.

An ideal microdosimeter should have a small radiation sensitive volume (SV) to yield microdosimetric quantities able to describe the biological damage in the cell content. It means that the SV should be designed with a well-defined cylindrical volume (Kellerer 1985, Rossi and Zaider 1996) containing the full charge collection, without charge sharing between adjacent electrodes. Regarding these features, gas-filled tissue equivalent proportional counters (TEPC) have been traditionally the gold-standard sensors in microdosimetry (Int ICRU 1983, Rossi and Zaider 1996). However, TEPCs have some disadvantages, e.g. *wall effects*, high voltage bias (kV), gas supply requirements, and particularly they work only in conditions of low irradiation fluence rates. New mini-TEPCs have improved their performance in the last years (Bianchi *et al* 2020). Albeit, they are still point-like and suffer pile-up effects under therapeutic fluence rates. These characteristics make them infeasible for daily clinical measurements. In contrast, silicon-based radiation detectors may overcome these disadvantages since they do not require gas supply, may work at low voltages, have fast response and high spatial resolution, and can be constructed in wall-less micrometer sizes. They have other limitations although, e.g. they are not water equivalent, their performance can deteriorate due to radiation damage over time, and their detection limit (as a function of their size) may be jeopardized by the electronic noise of the corresponding readout electronics (Prieto-Pena *et al* 2020). Even though, behind appropriate tissue-correction, they have contributed significantly to the microdosimetry verification in the last years. On the one hand, Rosenfeld (Univ. of Wollongong) and collaborators have created several different generations of them. The first four generations of microdetectors that they proposed are mainly based on either planar PN junctions with implantations on the front-face, or with those junctions with their silicon boundaries etched to avoid charge collection sharing (Bradley 2000, Rosenfeld 2016). They have been tested in PT successfully (Anderson *et al* 2017). In the last 5th generation, a similar configuration to our proposed 3D-cylindrical microstructures (detailed below) has been recreated in a clean-room facility in Norway in 2018 and tested in carbon ions (Tran *et al* 2018) and in low energy proton in 2020 (Samnøy *et al* 2020). In that structure, the SVs are separated into odd and even arrays and thus the signal is read jointly, which deteriorates the spatial resolution. Recently its performance has been compared with a mini-TEPC in a 62 MeV therapeutic modulated proton beam (Conte *et al* 2020). Although they found some discrepancies in the microdosimetry spectra, their RBE assessments led to consistent results. On the other hand, in Europe, (Bianchi *et al* 2020) has proposed a telescope detector with a matrix of pixels (2 μm in thickness) coupled with a deeper stage (about 500 μm in thickness) based on the previous design of the same group (Agosteo *et al* 2010).

In response to these issues, we aimed at creating, first, an ultra-thin 3D microdetector (Guardiola *et al* 2012, 2013, Gómez *et al* 2016) based on the 3D-architecture proposed by Parker *et al* (1997) and, secondly, a new 3D-cylindrical design (Guardiola *et al* 2015a) with sizes as those of cellular nuclei. Both architectures reduce the loss of charge carriers due to trapping effects, the charge collection time, and the voltage for full depletion, compared to planar silicon detectors (Guardiola *et al* 2020). Particularly, the last architecture with electrodes into the silicon bulk and very well delimited SV improves those features and mimics the shapes and sizes similar

than those of mammalian cells, whose diameters cover from 10 to 100 μm. From the best of our knowledge, there are not 3D-cylindrical microdetectors excepting those manufactured in the National Centre of Microelectronics (IMB-CNM, CSIC, Spain) specifically for microdosimetry (Guardiola *et al* 2015b, Fleta *et al* 2015, Prieto-Pena *et al* 2019a, 2020). The feasibility of the first 3D-cylindrical generation as microdosimeters has been recently demonstrated in a clinical carbon beam at the synchrotron of the Fondazione Centro Nazionale di Adronterapia Oncologica (CNAO, Italy) (Prieto-Pena *et al* 2019a).

While LET is calculated over the average energy deposited in large SV sizes, its equivalent microscopic quantity, the lineal energy (y), has a stochastic nature. Thus, estimates of LET can be based on lineal energy distribution probabilities. Lineal energy is calculated as the ratio between the energy deposited (ε) by particles impinging within the SV divided by the *mean chord length*, $\bar{l}$, of it (Int ICRU 1983):

$$y = \frac{\varepsilon}{l}. \tag{1}$$

The lineal energy values must be adjusted by two correction factors, namely (i) the charge collection efficiency (CCE) and (ii) the tissue equivalence, i.e. silicon to water conversion. Once the energy spectrum is obtained during the measurements, it is possible to generate the probability distribution of the lineal energy, $f(y)$. This is the microdosimetric quantity that allows for the RBE estimation that can be used for improving treatment planning systems. Once that the probability distribution $f(y)$ is known, the first moment of it (*frequency mean lineal energy)*, $\overline{y_F}$, can be calculated as:

$$\overline{y_F} = \int y f(y) \, dy. \tag{2}$$

Likewise, the dose weighted distribution, or microdosimetric dose distribution, may be expressed as a function of the lineal energy as:

$$d(y) = \frac{y f(y)}{\overline{y_F}}. \tag{3}$$

The mean value of this distribution is denoted by the dose-mean lineal energy, $\overline{y_D}$, which is calculated as:

$$\overline{y_D} = \frac{1}{\overline{y_F}} \int y^2 f(y) \, dy = \int y \, d(y) \, dy. \tag{4}$$

It represents better the damage to cells than the $\overline{y_F}$ since events with higher values of y are associated to higher efficiency of the radiation to produce biological damage. Further details about how to obtain the microdosimetry distributions can be found elsewhere (Kellerer 1985, Rossi and Zaider 1996).

In treatment planning, the product of the RBE and the physical dose is used to calculate the biological or RBE-weighted dose that considers not only the amount of radiation delivered to the target, but also many biological factors. For example, RBE can be calculated based on the MKM (Hawkins 2003), LEM (Grün *et al* 2012) and NanOx (Cunha *et al* 2017). In particular, if the measured dose-mean lineal energy ($d(y)$) is convolved with a biological response function ($r(y)$), we may obtain the corresponding RBE as (Loncol *et al* 1994):

$$\mathrm{RBE}(y) = \int r(y) d(y) \, dy. \tag{5}$$

In that way, we may calculate RBE from databases of both *in vitro* and *in vivo* data for different biological effects. It was validated first by Loncol *et al* (1994) for protons, high energy photons and neutrons, and later by Coutrakon *et al* (1997) in PT. For example, the RBE$_{10}$ can be calculated by using the modified MKM model that includes the cell survival determined by the lineal quadratic (LQ) model. The LQ model may provide both α and β cell radio sensitivity parameters for the particular radiation quality employed. Hence, RBE$_{10}$ is:

$$\mathrm{RBE}_{10} = \frac{2\beta D_{10,R}}{\sqrt{\alpha^2 - 4\beta \ln(0.1)} - \alpha} \tag{6}$$

$D_{10,R}$ is the dose required to obtain a 10% of cell survival for the specific cell line irradiated (with a radiation quality of reference, e.g. x-ray). Likewise α can be defined as a function of the lineal energy as:

$$\alpha = \alpha_0 \frac{\beta}{\rho \pi r_d^2} y^* \tag{7}$$

α_0 is the initial slope of the survival curve, ρ is the tissue density, r_d is the radius of the MKM sub-cellular domain (Hawkins 2003) and y^* is the restricted dose-mean lineal energy.

To our knowledge, the only work in the literature on the use of silicon-based 3D-cylindrical microdetectors under clinical conditions is from Prieto-Pena *et al* (2019a). The scarcity of publications is due to the fact that the emerging energy threshold during clinical measurements can be considerably higher than the perceptible y values delivered in clinical beams. Dose average lineal energy values in proton beams range
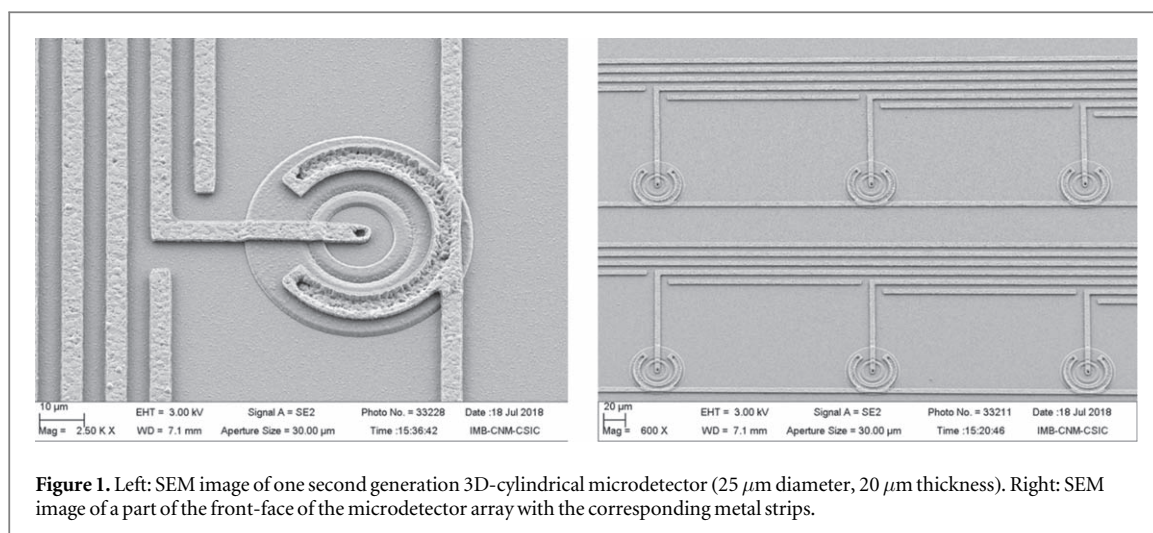
Figure 1. Left: SEM image of one second generation 3D-cylindrical microdetector (25 μm diameter, 20 μm thickness). Right: SEM image of a part of the front-face of the microdetector array with the corresponding metal strips.

from 1 to 2 keV μm^{-1}. Considering the SV thicknesses ($\leqslant$20 μm), the signal-to-noise (S/N) ratio becomes a challenge in those conditions.

We present the first microdosimetry measurements with low energy protons with the improved second generation of 3D-cylindrical microdetectors (25 μm diameter, 20 μm thickness) at clinical-equivalent fluence rates. We used a proton cyclotron beam in the National Accelerator Centre (CNA, Spain), which has started to be used for radiobiology studies (Baratto-Roldán *et al* 2018, 2020). Additionally, we introduced both corrections factors, first regarding a recent full CCE study (Barchiller-Perea *et al* 2020) of these second generation sensors and, secondly performing Monte Carlo simulations for accurate tissue-equivalent correction for low energy protons since it can vary at low energies (Agosteo *et al* 2010). Furthermore, we developed a low-noise readout electronics to improve the S/N ratio in clinical scenarios.
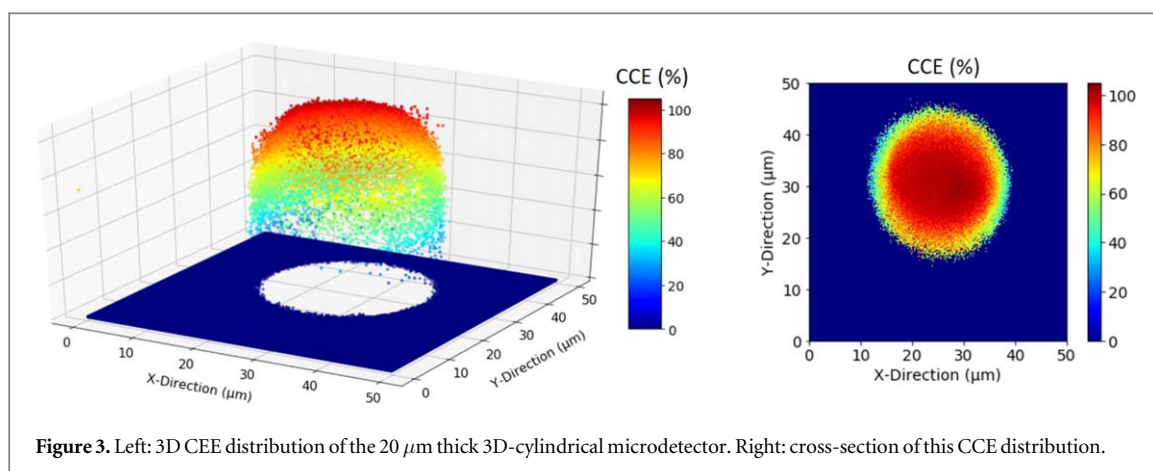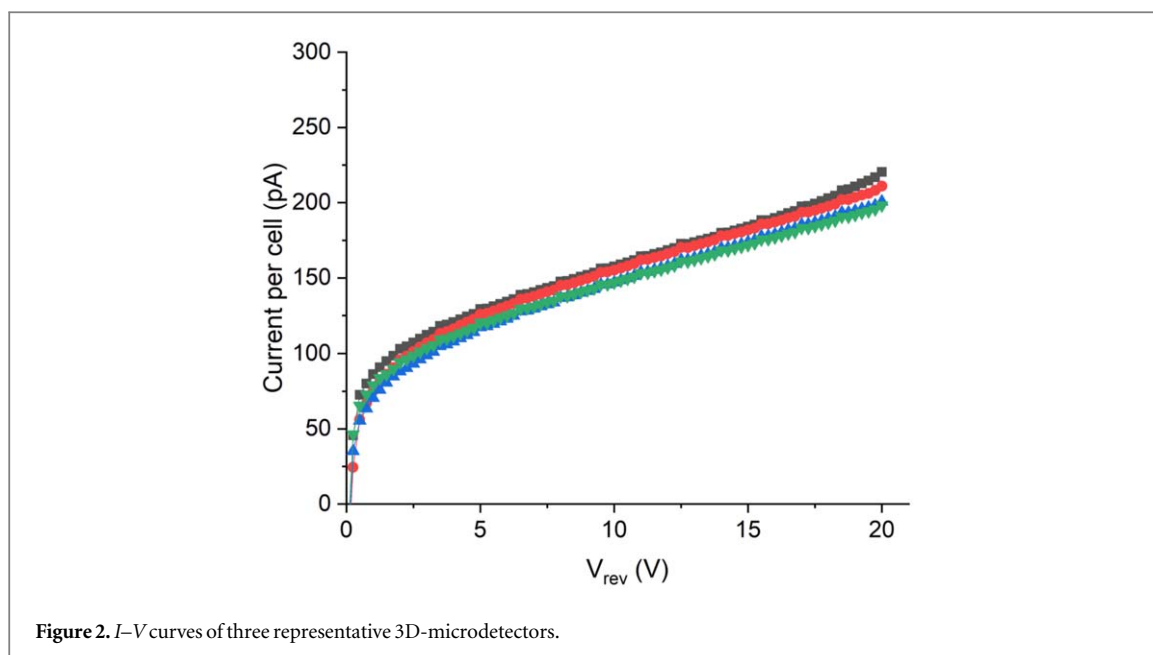
2. Materials and methods

2.1. Silicon 3D-cylindrical microdetectors

The first silicon-based 3D-cylindrical microdetectors were design and manufactured by the IMB-CNM (CSIC), Spain (Fleta *et al* 2015, Guardiola *et al* 2015a, 2015b, 2020), in 2013–2015. The second improved generation has been recently performed on 4 inch silicon-on-insulator (SOI) wafers. The device silicon is $\langle 100 \rangle$, n-type doped with phosphorus, with a nominal resistivity greater than 3.5 k$\Omega \cdot$ cm and nominal thicknesses of (10 $\pm$ 0.5) μm and (20 $\pm$ 0.5) μm. The base of the microfabrication technical details can be found elsewhere (Esteban 2016, Prieto-Pena 2019b). Several improvements have been performed in this second generation. One of the most important ones was the reduction of the overall thermal budget, especially of the Ohmic N$^+$ contact doping, in order to obtain shallower and steeper dopant profiles, which had a significant impact in the CCE improvement (Bachiller-Perea *et al* 2021). Figure 1 shows scanning electron microscope images of the top-view of second generation 3D-cylindrical microdetectors. Figure 1, left, displays the p- and- n electrodes. The p- type electrodes have a 4 μm diameter and are surrounded by a n- type annulus of 3 μm width. Each p-type electrode has independent readout. A 2.6 μm SiO$_2$ and Si$_3$N$_4$ passivation layer is deposited over the surface. The diameter of the SV used herein is 25 μm, but they can be manufactured down to 9 μm. Although these 3D-cylindrical microdetectors are distributed in a 11 $\times$ 11 array with pitches from 25 to 200 μm (figure 1, right), for the sake of simplicity, in this work we used only one SV with a single readout channel while the others were grounded. Bias voltage for full depletion was 5 V.

Figure 2 shows a representative *I–V* electrical characterization curve of some microdetectors for one of the manufactured wafers. Devices have leakage currents in the order of 100 pA/cell and capacitances of 80 fF/cell at 5 V.

The CCE of the devices has been studied by means of the ion beam induced charge (IBIC) technique for both 10 and 20 μm thicknesses and 25 μm diameter. The IBIC study was performed with He2+ ions. CCE results are independent of the charged particle used for the IBIC measurements. The energy of the He2+ ions was 5.0 MeV, depositing an energy in the SV of ~4.2 MeV, (calculated with SRIM code Ziegler *et al* 2010). This energy was chosen in order to have an ion range (21.4 μm) larger than the thickness of the detector to produce electron–hole charge carriers all along the depth of the device. The bias voltage was set at 10 V, the average ion flux was ~5 $\times$ 10^7 s^{-1} cm^{-2}, and the acquisition time was ~30 min. Figure 3 shows the 3D-CEE distribution of the 20 μm thick 3D-cylindrical microdetector. The CCE ranges between 100% and 90% for radial distances up to

Figure 2. *I–V* curves of three representative 3D-microdetectors.

Figure 3. Left: 3D CEE distribution of the 20 μm thick 3D-cylindrical microdetector. Right: cross-section of this CCE distribution.

10.75 μm from the center of these sensors, and it rapidly decays between 10.75 μm at the detector edge. Further details may be found in Bachiller-Perea *et al* (2021). The position dependent CCE falls to zero in the boundaries of the 3D-cylindrical volume biasing the reconstruction of the energy imparted per event. Thus, a correction factor was included in the Monte Carlo simulations below to take this effect into account (Prieto-Pena *et al* 2020).

2.2. Readout electronics

The electrical charge produced by a single proton event in silicon is typically of the order of 1–30 fC. Therefore, it must be amplified to be able to register it correctly. This was done by a combination of charge preamplifier, shaper, and amplifier electronics (Knoll 2010). The in-house electronics integrated those functions in a 35 mm × 170 mm portable printed circuit board (PCB) powered by ±12 V. Figure 4 shows the set-up of the single channel readout electronics created for increasing the S/N ratio. It consists of two PCBs: one houses the 3D-cylindrical microdetector and the charge preamplifier (figure 4, left), and the other includes the shaping and amplification stages far away (10 cm distance) to avoid irradiation damage (figure 4, right).

The charge preamplifier used an OPA657 amplifier, a device with a high-gain bandwidth, low-distortion, voltage-feedback operational amplifier with a low-voltage noise JFET-input stage offering a high dynamic range amplifier suitable for the very low level signals that the detector provides. The shaper houses an inverter fixed gain amplifier (HFA1112). After the inverter, a CREMAT CR-200 Gaussian shaping amplifier and a CREMAT CR-210 baseline restorer followed by a HA-5002 current buffer amplifier are used to drive the output signal (Prieto-Pena 2019b). The output was combined with a commercial multichannel pulse height analyser (MCA8000D) connected via USB to obtain and store the energy spectra.
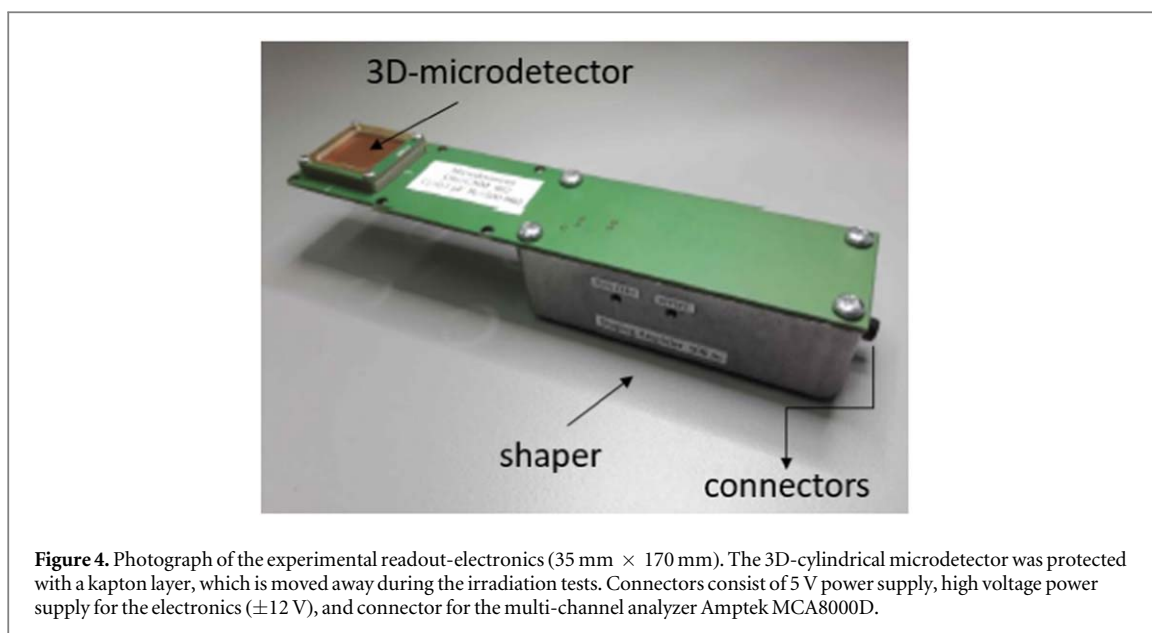
Figure 4. Photograph of the experimental readout-electronics (35 mm × 170 mm). The 3D-cylindrical microdetector was protected with a kapton layer, which is moved away during the irradiation tests. Connectors consist of 5 V power supply, high voltage power supply for the electronics (±12 V), and connector for the multi-channel analyzer Amptek MCA8000D.

An energy threshold (low level discrimination (LLD)) is set to avoid the electronic noise in such a way that only signals above this threshold are counted. It has to be as lower as possible to be able to quantify low lineal energy values. In our experiment, electronic noise may come from of pick-up noise from ubiquitous electromagnetic radiation caused by external devices. To avoid it and thus optimizing the S/N ratio, electronics were enclosed in two partial Faraday cages: the shaper was covered by a standard aluminum cage (figure 4, right), while 3D-microdetectors were surrounded by gold-metallized frames with an open window for the particle entrance (figure 4, left). LLD was fixed at (2.5 ± 0.5) keV μm^{-1} to discard low energy counts from the radiation background.

2.3. Experimental set-up

Irradiations were performed in the cyclotron facility (Cyclone 18/9 model) of the CNA. It has an external beamline for interdisciplinary research purposes and accelerates protons and deuterons to 18 and 9 MeV, respectively. Although the energy of these beams is below the energy range used in clinical PT (up to 230 MeV), this study is acceptable as first approach since 18 MeV proton beams arrive into the Bragg peak of nominal energy-equivalent clinical beams. The Bragg peak curve was sampled taking spectra in independent steps by using tungsten foils from 50 to 300 μm thickness with 10% ($> 50\ \mu$m) and 15% ($\leqslant 50\ \mu$m) relative uncertainties according to the manufacturer (Goodfellow Cambridge Ltd, Huntingdon, England) at the exit-window of the external beamline, which results in different energies of the proton beam arriving to the sensor. The front-face of the microdetector SV (see figure 1) was placed in a perpendicular plane to the propagation direction of the proton beam.

The 18 MeV (0.14 MeV experimental energy spread (σ_{exp})) proton beam arrives horizontally to the experimental room via the beam transport system, consisting of a variable graphite slit, an XY magnetic steerer, a quadrupole doublet and a quadrupole singlet. A two meter thick concrete wall, through which a stainless steel vacuum pipe transports the beam, separates the cyclotron bunker from the experimental room, where the beam is finally extracted into the air through the exit-window (Baratto-Roldán *et al* 2018). An unfocused beam was used, broadened with a 500 μm thick Aluminum scattering foil and 100 μm of Mylar. It yields an exit energy of the proton beam of 14.49 MeV (0.19 MeV σ_{exp}). For the sake of clarification, the beam diagnostics was developed at the exit of the beamline by measuring the beam energy distributions and lateral profiles and comparing them with Monte Carlo simulations. On the one hand, a set of Monte Carlo simulations were performed initializing the beam as a point-like source with a Gaussian energy distribution. A fixed initial proton beam energy of 18 MeV was used, changing the initial standard deviation (σ) from 0.18 MeV (nominal value) to 0.10 MeV in steps of 10 keV. On the other hand, measurements were carried out with a lithium-drifted silicon detector (L-040-075-5, ORTEC, Oak Ridge, Tennessee, USA). Then, the best agreement between measured and simulated energy spectra was obtained with a Gaussian energy distribution with a mean value of 18.00 ± 0.14 MeV (Baratto-Roldán *et al* 2020). Starting from this reference value, another simulation with the additional foils described above was performed and we obtained a Gaussian distribution with a mean value of 14.49 ± 0.19 MeV. The proton beam stability and intensity were verified by an graphite Faraday cup coated with a ZnS(Ag)

Table 1. From left to right: tungsten foil thicknesses placed at the exit-window of the external beamline and the corresponding WET. Simulated mean values of the proton beam energies delivered by the cyclotron right before the SV front-face (after the sensor passivation layer).

W foil thickness (μm)	WET (mm)	Mean energy at the SV entrance (MeV)
0	0	13.5 (0.2 σ)
50 $\pm$ 8	0.40 $\pm$ 0.08	12.0 (0.6 σ)
100 $\pm$ 16	0.79 $\pm$ 0.13	10.3 (0.7 σ)
150 $\pm$ 24	1.2 $\pm$ 0.2	8.4 (0.8 σ)
200 $\pm$ 20	1.6 $\pm$ 0.2	6.1 (1.0 σ)
250 $\pm$ 28	1.9 $\pm$ 0.3	3.1 (1.5 σ)
300 $\pm$ 30	2.2 $\pm$ 0.4	1.9 (1.6 σ)

scintillator, allowing us to see the beam position and measure its fluence. This Faraday cup is in vacuum, one meter from the exit-window and is remotely controlled from the control room.

Once the extraction conditions are as desired, we made use of variable slits that are located in the cyclotron vault. The beam intensity was adjusted from the minimum obtained with the cyclotron source (a few tens of pA) to the intensities that the detector can measure without damaging it. The final beam flux was measured by integrating the number of counts in the spectrum and dividing by the the front-face area of the 3D-microdetector SV and acquisition time. The average fluence rates were around $3 \times 10^7 \, \text{s}^{-1} \, \text{cm}^{-2}$, which is of the order of magnitude as the rates used in clinical scenarios. Measurements were carried out in air at room temperature and at a distance of 24 cm from the detector front-face to the exit-window of the external beamline. Spectra were recorded at 7 depths along the Bragg curve by adding the tungsten foils progressively (see table 1).

2.4. Monte Carlo simulations

Simulations were performed with a Geant4-based Monte Carlo (MC) code, namely the GATE (Sarrut *et al* 2014) open-source, to crosscheck the pulse height spectrum measurements. The irradiation configurations as well as the microdetector described in sections 2.1 and 2.3 were simulated with the GATE v8.1 version. The physics lists and parameters recommended by the GATE collaboration for PT applications were used, namely the Binary Cascade (BIC) model for the hadronic interactions adding the G4EmStandardPhysics_option3 to describe electromagnetic interactions (Agostinelli *et al* 2003, Geant4 Collaboration 2020). These options were included with the QGSP_BIC_HP_EMY *GATE-build*er. Range cuts of 1 mm, 1 μm, and 0.5 μm were considered for all the particles for the *world*, SV, and passivation layer geometries respectively. The ionization potentials for water and air were 78 eV and 85.7 eV respectively. It is worth noting that the densities of the SiO_2 and Si_3N_4 passivation layers (section 2.1) when they are deposited by plasma-enhanced chemical vapor depositions processes have average values of 2.3 g • cm^{-3} and 2.6 g • cm^{-3} respectively (Adams *et al* 1981, Gupta *et al* 1991). These were the values considered in the simulations.

The proton source was modeled as a general particle source regarding the beam features described above. A Gaussian shape for the energy spectrum was simulated with a mean energy value of 14.49 MeV and a standard deviation of 0.19 MeV. Several simulation sets were performed with the respective tungsten foil thicknesses displayed in table 1. The number of simulated primary protons was 5×10^{11} in each set, which delivers an average statistical uncertainty lower than 1%. The total energies deposited into the SV of the 3D-cylindrical microdetector were recorded and consequently the lineal energy distributions were calculated by dividing the energies spectra by the mean chord length (see equation (1)). The mean chord length was equal to the final manufactured SV thickness, namely 19.6 μm, for irradiations that are perpendicular to the sensor surface, such as the configuration studied herein. Simulations also took into account the energy resolution that is 12% full width at half maximum at 660 keV (Prieto-Pena *et al* 2019a). Once the simulated energy spectra were obtained, they were treated to account for the CCE dependence on the entry point of the particle trajectory to the SV as follows: a random position in a circle of 25 μm radius centered in the SV was assigned for each of the points. Then, the CCE correction factor for each point was applied by using the measured CCE (Bachiller-Perea *et al* 2021) (see figure 3) as a function of distance to the center of the SV. Finally, the energy spectra were reconstructed and compared with experimental data. Afterwards, the microdosimetry distributions were assessed as described elsewhere (Kellerer 1985, Rossi and Zaider 1996).
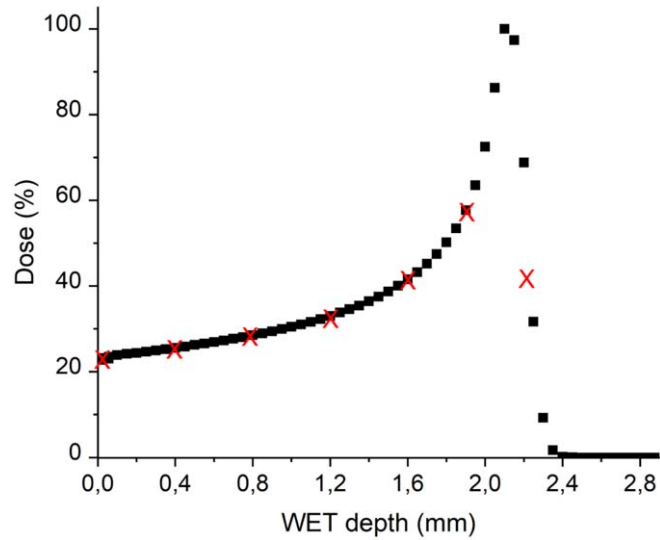
Figure 5. Simulated percentage of depth dose curve as the initial 14.49 MeV (0.19 MeV σ_{exp}) proton beam impinges on a water phantom. Red crosses correspond to the experimental point positions.

3. Results

Table 1 summarizes the mean energy values of the proton beam when impinging on the SV entrance. These values were also obtained with the MC simulations as it is described above. Table 1 also includes the water equivalent tissue (WET) thicknesses corresponding to each W foil thickness. WET gives the water thickness that produces the same energy loss than that in the W foils. It was calculated as described in Zhang *et al* (2010):

$$\mathrm{WET} = t \cdot (\rho_{\mathrm{m}}/\rho_{\mathrm{w}}) \cdot (S_{\mathrm{m}}/S_{\mathrm{w}}). \qquad (8)$$

Being t the tungsten foil thickness, and ρ_{m}, ρ_{w}, S_{m}, and S_{w} the tungsten and water densities and mean mass stopping powers, respectively. The mean stopping powers were integrated over the total depth by interpolating first the corresponding values for thickness steps of 12.5 μm, which is the fourth part of the first W foil thickness and for which the standard deviation of the corresponding stopping power ratios was below of 4%, and secondly by integrating them in the total range. The mean mass stopping power values were obtained from the PSTAR database (Berger *et al* 1999).
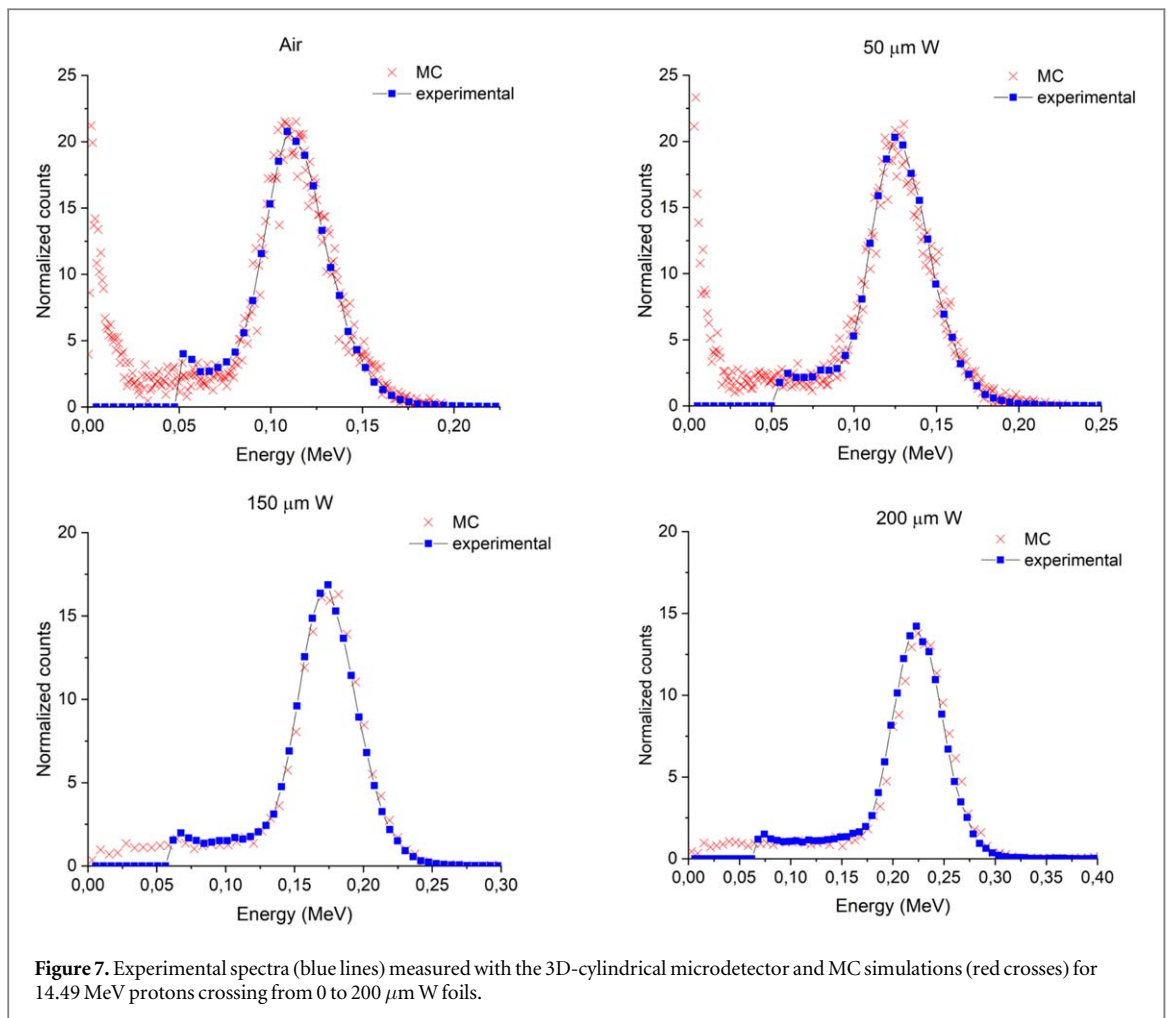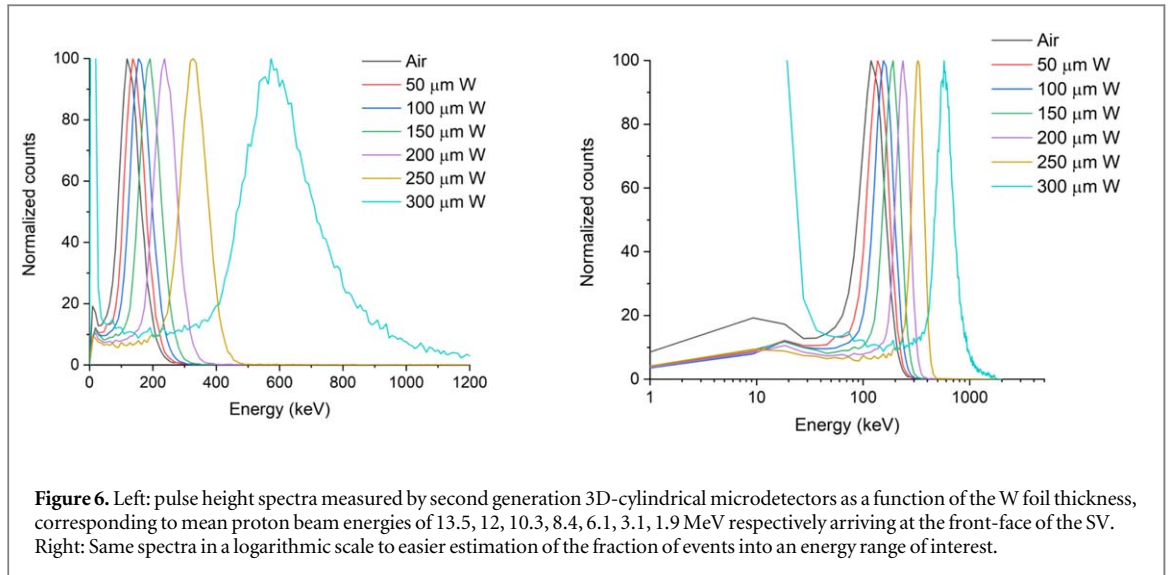
The proton beam energy had a Gaussian profile when arriving to the SV since the initial beam (14.49 MeV with 0.19 MeV σ_{exp}) was characterized with that type of distribution (Baratto-Roldán *et al* 2018). As it is expected, the thicker the W foil, the lower the mean proton energy and the wider the energy spread.

Figure 5 shows the simulated percentage of depth dose curve (PDD) in water for the initial 14.49 MeV (0.19 MeV σ_{exp}) proton beam. Regarding it, the measurement points of the table 1 that correspond to water depths are placed at the PDD entrance (1.2 mm $\leqslant$ WET), proximal distance (1.6 mm WET), close to the Bragg peak (1.9 mm WET), and distal edge (2.2 mm WET), respectively. These points are highlighted with red crosses in figure 5.

Nevertheless, it is worth noting that since the foil positions are 22.7 cm away from the SV, these equivalent-positions into the PDD are shifted deeper since the loss energy along the track in air is not negligible at those proton low-energies.
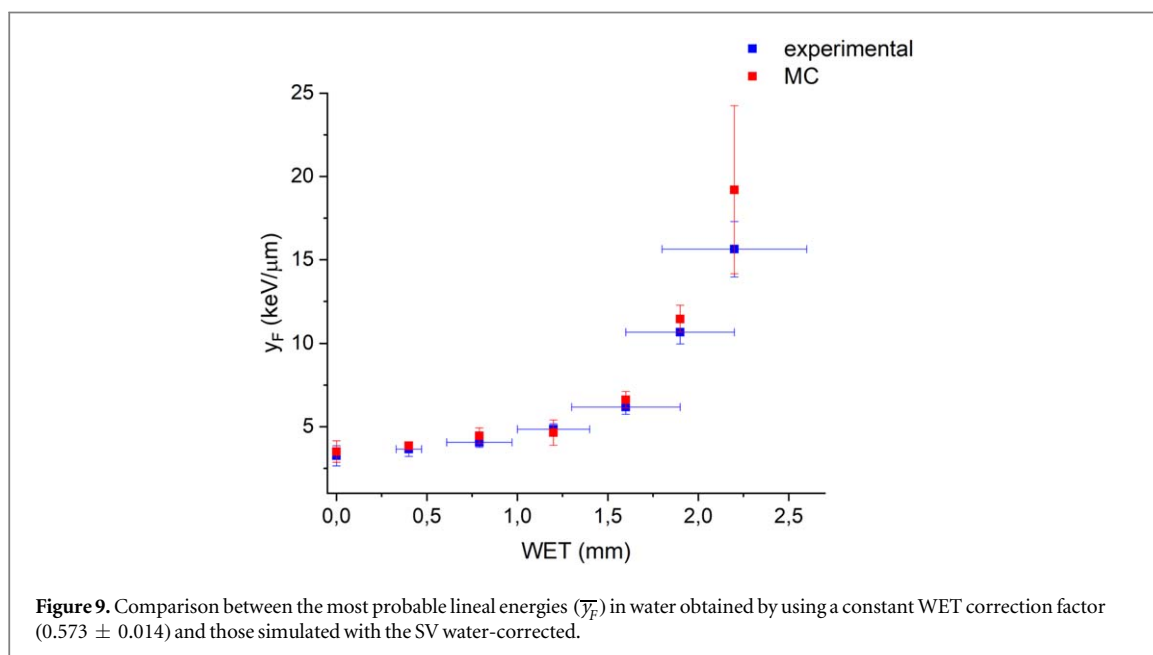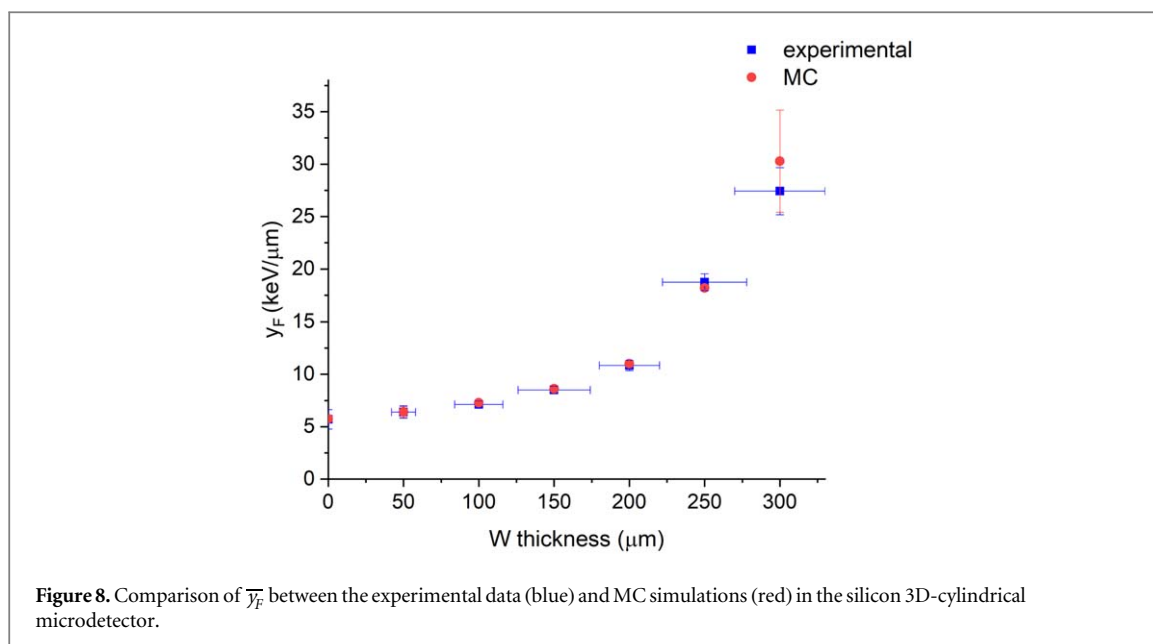
Figure 6 shows the pulse height spectra measured by a second generation 3D-cylindrical microdetector of 25 μm diameter and 19.6 μm thickness as a function of the W foil thickness along the Bragg curve. The pulse height spectra show the following features: (i) since the mean proton beam energy decreases as the tungsten thickness increases, a different pulse height spectrum is generated for each depth and consequently the most probable lineal energy increases and the spectra shift to higher energies as we approach to the distal edge; (ii) the spectra distributions are broader at low proton energies due to the straggling produced when protons cross the W foils; and (iii) the main peak comes mainly from the central region of the SV and the low pulse-height events (tail on the left of the spectra) are originated at the periphery of the detector, as it was explained in Bachiller-Perea *et al* (2021).

Figure 7 shows the comparison between some of these experimental spectra and those simulated for a the 3D-cylindrical microdetector for the different W foil thicknesses. The agreement between both experimental and simulated data is remarkable. A small peak position shift was found between the original simulated energy distributions and the ones calculated applying the CCE correction factors. This shift varies in value all along the

Figure 6. Left: pulse height spectra measured by second generation 3D-cylindrical microdetectors as a function of the W foil thickness, corresponding to mean proton beam energies of 13.5, 12, 10.3, 8.4, 6.1, 3.1, 1.9 MeV respectively arriving at the front-face of the SV. Right: Same spectra in a logarithmic scale to easier estimation of the fraction of events into an energy range of interest.

Figure 7. Experimental spectra (blue lines) measured with the 3D-cylindrical microdetector and MC simulations (red crosses) for 14.49 MeV protons crossing from 0 to 200 μm W foils.
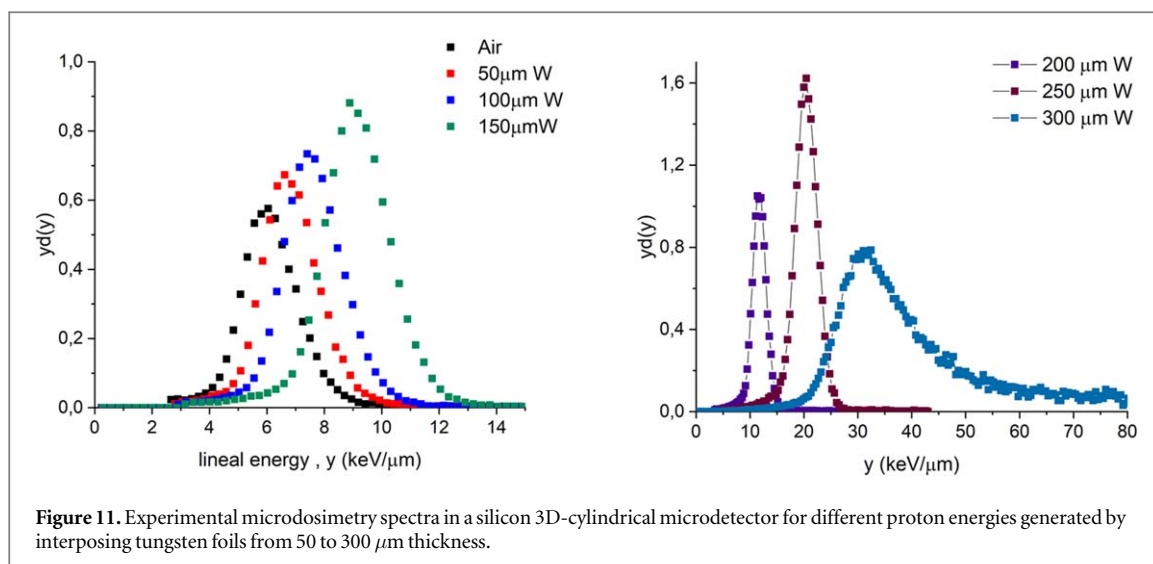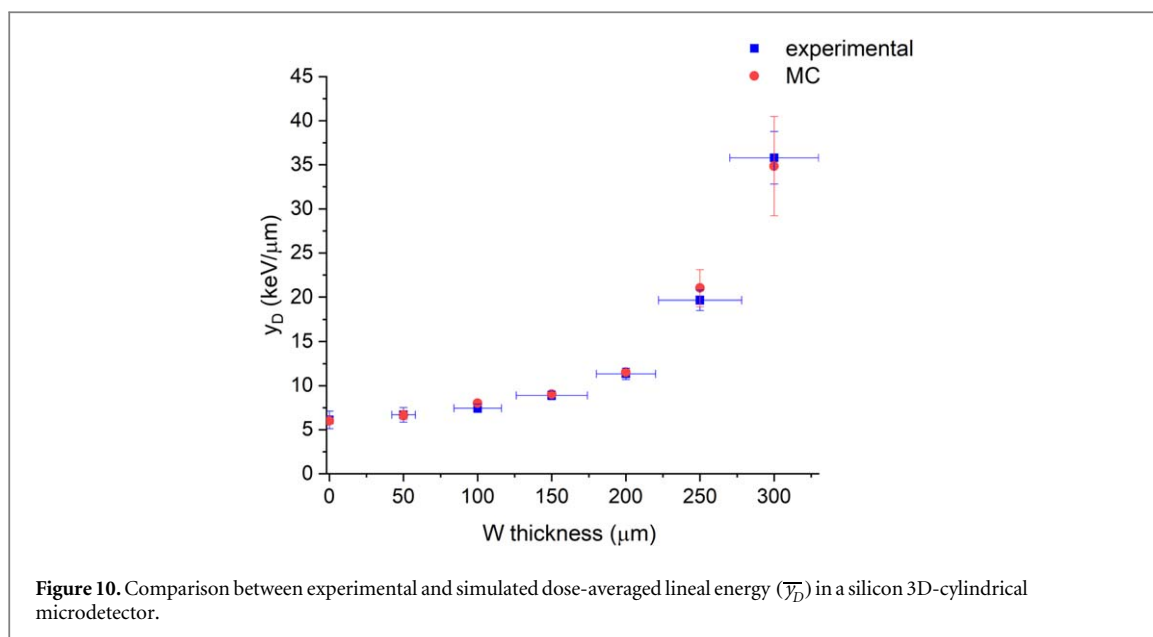
Bragg curve and is proportional to the energy deposited in the detector. This peak shift was also found in a previous work (Prieto-Pena *et al* 2020) with the first generation 3D-cylindrical microdetector, even though in this version the mean shift is smaller (4%) than with the previous generation of microdetectors (6%).

Figure 8 shows a very good agreement considering the error bars between the experimental and simulated frequency mean lineal energy, $\overline{y_F}$ (see equation (2)), in silicon, for all the W foil thicknesses. The experimental $\overline{y_F}$ values in silicon cover from (5.7 ± 0.9) to (8.5 ± 0.4) keV μm^{-1} at the entrance, (10.9 ± 0.5) keV μm^{-1} at the proximal distance, to (18.7 ± 0.8) keV μm^{-1} close to the Bragg peak and (27.4 ± 2.3) keV μm^{-1} at the distal

Figure 8. Comparison of $\overline{y_F}$ between the experimental data (blue) and MC simulations (red) in the silicon 3D-cylindrical microdetector.

Figure 9. Comparison between the most probable lineal energies ($\overline{y_F}$) in water obtained by using a constant WET correction factor (0.573 ± 0.014) and those simulated with the SV water-corrected.

edge. The relative differences with the respective MC simulations were lower than 3%, except for the last point that reached 10%. It may be due to two reasons: first, a possible misalignment between the front-face of the SV microdetector and the propagation direction of the beam that might change the mean chord length and thus the moments of the probability distribution; secondly, while simulations were performed with a fixed W thickness for each point, the experimental W thickness uncertainties were not insignificant (see table 1). This W thickness difference between the current and simulated foils might have a high impact in the energy spectra and therefore in the final $\overline{y_F}$ evaluation.

   Figure 9 shows the experimental and simulated $\overline{y_F}$ in water for the corresponding depths in WET (see table 1). It is worth noting that the experimental $\overline{y_F}$ in water was calculated considering a constant correction factor of tissue equivalence, namely (0.573 ± 0.014), as studied by (Bradley 2000) for all the points. However, according to Agosteo *et al* (2010), when the mean proton beam energy is lower than 6.5 MeV, the use of this constant correction factor produces a disagreement with the experimental data as comparing with silicon-based microsensors and TEPCs. This is due to the fact that the mean mass stopping power ratio changes drastically at low energies and consequently a variable correction factor is more appropriate. In particular, for these mean proton energies (see table 1), the silicon-to-water stopping power ratio varies by up to a 12% (calculated from the PSTAR database) (Berger *et al* 1999). In order to study this possible disagreement, we performed a set of MC

Figure 10. Comparison between experimental and simulated dose-averaged lineal energy ($\overline{y_D}$) in a silicon 3D-cylindrical microdetector.

Figure 11. Experimental microdosimetry spectra in a silicon 3D-cylindrical microdetector for different proton energies generated by interposing tungsten foils from 50 to 300 μm thickness.

simulations to obtain the microdosimetry spectra in water for all the depths, which are represented by the MC values displayed in figure 9, following the methodology detailed by Magrin (2018).

The experimental $\overline{y_F}$ values in WET covered from (3.3 ± 0.6) to (4.9 ± 0.3) keV μm^{-1} at the entrance, (6.2 ± 0.4) keV μm^{-1} at the proximal distance, to (10.7 ± 0.7) keV μm^{-1} close to the Bragg peak and (15.6 ± 1.7) keV μm^{-1} at the distal edge. Results shows that the $\overline{y_F}$ values simulated in a SV water-corrected were up to 10% higher in most of the points and 22% at the distal edge than those experimental using a constant water correction factor of (0.573 ± 0.014).

In figure 10 the dose-averaged lineal energy ($\overline{y_D}$) distributions in silicon (see equation (4)) are depicted. Both experimental and simulated $\overline{y_D}$ values in silicon cover from 6 to 9 keV μm^{-1} at the entrance, 11 keV μm^{-1} at the proximal distance, to 20 keV μm^{-1} close to the Bragg peak and 36 keV μm^{-1} at the distal edge. The relative differences with the respective MC simulations were lower than 3% in all the cases except for the 100 and 250 μm W foils that rise up to 8%.

Finally, figure 11 shows the microdosimetric distributions calculated with equation (3) using the energy spectra above (figure 6). They are traditionally plotted as $yd(y)$ versus the lineal energy. Microdosimetric distributions widen towards higher linear energy values when decreasing the proton beam energy. Figure 11 left, shows that the $yd(y)$ values at the entrance (1.2 mm $\leqslant$ WET) cover from 4 to 12 keV μm^{-1}. Figure 11 right, shows that the $yd(y)$ values at the proximal (1.6 mm WET) cover from 8 to 15 keV μm^{-1}, close to the Bragg peak (1.9 mm WET) from 14 to 26 keV μm^{-1}, and at the distal edge (2.2. mm WET) they expand up to 60 keV μm^{-1}.

4. Discussion

In early works we used a 3D microdetector configuration, namely ultra-thin 3D silicon detectors, for the first microdosimetry measurements at a cyclotron proton beamline (Guardiola *et al* 2015c) and in a carbon clinical center (Gómez *et al* 2016). However, these first results led to suggest important technological and spatial resolution improvements. Hence, we proposed a new architecture of radiation silicon-based detectors, called 3D-cylindrical (Guardiola *et al* 2015b, 2020). With our novel 3D-cylindrical architecture, we obtained a better well-defined convex SV that contains the full charge collection, without charge sharing between adjacent electrodes, and the highest spatial resolution so far by having a pixel-type configuration that allows for independent readouts of each 3D-cylindrical microdetector. In this sense, for example, the Rosenfeld's group microdosimeters do not have a matrix of microsensors with multiplex channels of independent readouts, and therefore their performances are limited in spatial resolution and cannot generate LET 2D-maps. Additionally, in their works they have not included the CCE correction factor, which is a general problem for solid-state structures. From the best of our knowledge, we have included for the first time the CCE factor in the reconstruction of the imparted energy into the detector active volume. Each event pulse height is here considered as the convolution of the actual energy deposition along the silicon detector with the effective CCE map. It is worth noting that the construction of buried silicon structures for microdosimetry using any technique of microfabrication would yield similar effects on the CCE problems whenever the volumes considered are in the range of micrometers. We explained the importance of this issue in Prieto-Pena *et al* (2020). This 3D-cylindrical design also reduces the drifting distance and collection times of charge carriers generated by the radiation due to its micrometer size compared with standard planar detectors (Pellegrini *et al* 2013). It provides micro-SV with sizes and shapes similar than those of mammalian cells, whose diameters cover from 10 to 100 μm. Additionally, the microfabrication on SOI wafers allows us for removing the support wafer to avoid potential backscattering or additional unwanted contributions to the measurement of energy deposition. We have studied the suitability of the second generation of improved 3D-cylindrical microdetectors assembled with a customized readout electronic system. In particular, two main characteristics have been improved in the device presented here: its CCE and the S/N ratio (SNR).

Regarding the CCE, in the first generation an improvable CCE was reported and its impact over the microdosimetric spectra was discussed in Prieto-Pena *et al* (2020). Partially depleted SV can be due to the silicon 3D-cylindrical structure because of the intrinsic technological limits in the microelectronics manufacturing processes. It might lead to recombination of the ionization charge and therefore partial charge collection in the output signal. A limited CCE rises discrepancies between experimental and simulated data due to the reduced collected charge into de SV with respect to the full ideal collection in the MC simulations. However, in the second generation, the CCE has considerably improved due to the microfabrication enhancements, mainly the reduction of the thermal budget of the N^+ Ohmic contacts, leading to shallower and steeper dopant profile. The CCE ranged between 100% and 90% for radial distances up to 10.75 μm from the center of the device, and it rapidly decays between 10.75 μm and the detector edge, consequence of a steeper dopant profile. A relative active volume of (96.2 ± 0.6)% with respect to the nominal design was obtained thanks to the shallower Ohmic regions. It is a considerable enhancement with respect to the first generation where the active volume was 56% (Fleta *et al* 2015). When computing the lineal energy, CCE variations in the SV can be translated to effective reduced chord length, thus to a modified probability density function of the effective chord length. It had a direct impact in the accuracy of reconstruction of microdosimetric spectra that were seriously compromised before in the low lineal energy region due to the low CCE at the SV periphery (Prieto-Pena *et al* 2020). In the first generation, the experimental pulse height distributions showed a relevant tail in the low-energy region of the spectra due to the partial CCE in the sensor periphery, which does not appear in the second generation. Another effect of the increase in the relative active volume with respect to the nominal design is that the peak shift observed between the original and the CCE-corrected energy deposition spectra is reduced compared to the previous generation of microdetectors (shift from 4% to 6 %). In spite of this, the microdetector response is independent of the proton beam energy, at least in the range covered here, as the excellent agreement with the simulations shows. Nevertheless, in order to obtain tissue equivalent microdosimetry spectra, it is necessary to integrate a water-to-silicon correction factor that is energy dependent at low energies. It may be particularly critical to the correct RBE evaluation in clinical scenarios where low energy beams fall into the distal edge. Although protons are low-LET particles, their LET sharply increases at the end of their range, as it is shown in figure 10.

Regarding the SNR, since it is rather inversely proportional to the square root of the total capacitance, we used a 3D configuration whose capacitance is two orders of magnitude lower than a traditional planar configuration and is more favorable for SV thicknesses lower than 50 μm (Pellegrini *et al* 2013). Additionally, an in-house low noise readout-electronics allowed us to have negligible contributions and to fix the LLD at (2.5 ± 0.5) keV μm^{-1} in silicon, which is approximately equivalent to (1.4 ± 0.3) keV μm^{-1} in WET. This

makes our device feasible for proton beam microdosimetry measurements whose lineal energy values for proton beams starts from 1 to 2 keV μm^{-1}. Measurements were performed with average therapeutic-equivalent fluence rates of around 3×10^7 s^{-1} cm^{-2} and neither pile-ups nor saturation effects were found.

Dose-mean lineal energy ($\overline{y_D}$) in silicon ranged from 6 to 9 keV μm^{-1} in the entrance, 11 keV μm^{-1} in the proximal distance, to 20 keV μm^{-1} close to the Bragg peak and 36 keV μm^{-1} in the distal edge. The relative differences with the respective MC simulations were lower than 3% in all the cases except for the 100 and 250 μm W foils that rise up to 8%. This difference may be due to two possible uncertainties: either the W thickness uncertainty or a misalignment of the SV. On the one hand, the W thickness uncertainties were 10% and 15% (for foils with thickness >50 μm and ⩽50 μm respectively). Since we used combinations of different W foil thicknesses, the uncertainty reached relative high values as it is shown in table 1. By contrast, simulations were performed with a fixed W thickness for each point. This difference between the simulated and real geometry of those foils might have a high impact in the energy spectra and therefore in the final $\overline{y_D}$ evaluation. The experimental data were restricted to few points due to the limited W foil thicknesses. This issue will be figure out with a new WET phantom with a micrometer stepper that we have manufactured for incoming tests. On the other hand, a possible misalignment between the front-face of the SV microdetector and the propagation direction of the beam that might change the mean chord length and thus the moments of the probability distribution. This issue will be minimize by placing the set-up on a tailored mechanical frame on a micrometer stepper.

Since the reference material in PT for dosimetry is the water, it was considered herein as the WET instead of tissue-equivalent, which was the traditional material used in microdosimetry due to the extended use of TEPCs. We compared the $\overline{y_F}$ in WET generated from those obtained in silicon by using both variable and average constant (0.573 ± 0.014) correction factors. Results showed that a variable WET correction factor must be considered at low proton beam energies since the use of a single scaling factor at the distal edge produce disagreements from 10% to 22%. It has to be carefully studied in clinical beams, e.g. SOBP with proton energies above 100 MeV, where there are mixed spectral fluencies and low energy contributions that may make an impact in the final $d(y)$ calculation.

Additionally, results show the good performance of the 18 MeV proton external beamline at CNA for microdosimetry applications and further radiobiology studies.

5. Conclusions

We carried out the first microdosimetric measurements with low energy proton beams with an improved 3D-cylindrical silicon-based microdetector. The second generation of 3D-cylindrical microdetectors have shown a better S/N ratio and CCE than the first one. Additionally, measurements at various depths along the Bragg curve of a 18 MeV cyclotron proton beamline were performed at therapeutic-equivalent fluence rates (around 3×10^7 s^{-1} cm^{-2}) without pile-up and saturation effects. Microdosimetry spectra were obtained and crosschecked with Monte Carlo simulations finding an excellent agreement.

This work consolidates the capability of the new 3D-cylindrical architecture as microdosimeters to characterize proton beams with therapeutic-equivalent proton fluence rates. Therefore, these devices can be used in PT and allow for further RBE calculations as well as commissioning under clinical conditions.

Acknowledgments

ORCID iDs

C Guardiola ⓘ https://orcid.org/0000-0002-0174-7451
D Bachiller-Perea ⓘ https://orcid.org/0000-0002-4447-9194
M C Jiménez-Ramos ⓘ https://orcid.org/0000-0001-7109-1040
J García López ⓘ https://orcid.org/0000-0003-4107-4383
C Fleta ⓘ https://orcid.org/0000-0002-6591-6744
D Quirion ⓘ https://orcid.org/0000-0002-5309-0535

References

Agostinelli S *et al* 2003 Geant4-a simulation toolkit *Nucl. Instrum Methods Phys. Res.* A **506** 250–303

Agosteo S, Cirrone G A P, Colautti P, Cuttone G, D'Angelo G, Fazzi A, Introini M V, Moro D, Pola A and Varoli V 2010 Study of a silicon telescope for solid state microdosimetry: preliminary measurements at the therapeutic proton beam line of CATANA *Radiat. Meas.* **45** 1284–9

Adams A C *et al* 1981 Characterization of plasma-deposited silicon dioxide *J. Electrochem. Soc.* **128** 1545

Anderson S E *et al* 2017 Microdosimetric measurements of a clinical proton beam with micrometer-sized solid-state detector *Med. Phys.* **44** 6029–37

Baratto-Roldán A, Jiménez-Ramos M C, Battaglia M C, García-López J, Gallardo M I, Cortés-Giraldo M A and Espino J M 2018 Feasibility study of a proton irradiation facility for radiobiological measurements at an 18 MeV cyclotron *Instruments* **2** 26

Baratto-Roldán A, Jiménez-Ramos M C, Jimeno S, Huertas P, García-López J, Gallardo M I, Cortés-Giraldo M A and Espino J M 2020 Preparation of a radiobiology beam line at the 18 MeV proton cyclotron facility at CNA *Phys. Med.* **74** 19–29

Bachiller-Perea D, García-López J, Jiménez-Ramos M C, Gómez F, Fleta C, Quirion D, García-Osuna A and Guardiola C 2021 Characterization of the charge collection efficiency in silicon 3D-detectors for microdosimetry *IEEE Trans. Instrum. Meas.* **70** 1–11 6005211

Bradley P D 2000 The development of a novel silicon microdosimeter for high LET radiation therapy *PhD Thesis* University of Wollongong

Berger M J, Coursey J S, Zucker M A and Chang J 1999 *ESTAR, PSTAR, and ASTAR: Computer Programs for Calculating Stopping-Power and Range Tables for Electrons, Protons, and Helium Ions* (version 1.2.3) National Institute of Standards and Technology, Gaithersburg, MD http://physics.nist.gov/Star

Bianchi A, Selva A, Colautti P, Bortotd D, Mazzucconid D and Polad A 2020 Microdosimetry with a sealed mini-TEPC and a silicon telescope at a clinical proton SOBP of CATANA *Radiat. Phys. Chem.* **171** 108730

Conte V *et al* 2020 Microdosimetry of a therapeutic proton beam with a mini-TEPC and a MicroPlus-bridge detector for RBE assessment *Phys. Med. Biol.* **65** 245018

Coutrakon G, Cortese J, Ghebremedhin A, Hubbard J, Johanning J, Koss P, Maudsley G, Slater C R and Zuccarelli C 1997 Microdosimetry spectra of the Loma Linda proton beam and relative biological effectiveness comparisons *Med. Phys.* **24** 1499–506

Cunha M, Monini C, Testa E and Beuve M 2017 NanOx, a new model to predict cell survival in the context of particle therapy *Phys. Med. Biol.* **62** 1248–68

Esteban S 2016 Development of advanced silicon sensors for neutron detection and microdosimetry *PhD Thesis* Universitat Autònoma de Barcelona

Fleta C, Esteban S, Baselga M, Quirion D, Pellegrini G, Guardiola C, Cortés-Giraldo M A, García-López J, Jiménez Ramos M C and Gómez F 2015 3D cylindrical silicon microdosimeters: fabrication, simulation and charge collection study *J. Instrum.* **10** P10001

Geant4 Collaboration 2020 Physics Reference Manual, Release 10.4 https://geant4.web.cern.ch/collaboration

Gómez F *et al* 2016 Measurement of carbon ion microdosimetric distributions with ultrathin 3D silicon diodes *Phys. Med. Biol.* **61** 4036–47

Guan F G *et al* 2018 RBE model-based biological doseoptimization for proton radiobiologystudies *Int. J. Part. Ther.* **5** 160–71

Gutierrez A *et al* 2019 The impact of proton LET/RBE modeling and robustness analysis on base-of-skull and pediatric craniopharyngioma proton plans relative to VMAT *Acta Oncol.* **58** 1765–74

Guardiola C, Fleta C, Pellegrini G, García F, Quirion D, Rodríguez J and Lozano M 2012 Ultra-thin 3D silicon sensors for neutron detection *J. Instrum.* **7** P03006

Guardiola C, Gómez F, Fleta C, Rodríguez J, Quirion D, Pellegrini G, Lousa A, de Olcoz A L, Pombar M and Lozano M 2013 Neutron measurements with ultra-thin 3D silicon sensors in radiotherapy treatment room using a siemens primus linac *Phys. Med. Biol.* **58** 3227–42

Guardiola C, Pellegrini G, Lozano M, Fleta C, Quirion D and Gómez F 2015a Microdosimeter based on 3d semiconductor structures, method for producing said microdosimeter, and use of said microdosimeter. International publication numberWO2015114193-A1 (06/08/2015) https://digital.csic.es/bitstream/10261/135459/1/WO2015114193A1.pdf

Guardiola C, Quirion D, Pellegrini G, Fleta C, Esteban S, Cortés-Giraldo M A, Gómez F, Solberg T, Carabe A and Lozano M 2015b Silicon-based three-dimensional micro-structures for radiation dosimetry in hadrontherapy *Appl. Phys. Lett.* **107** 023505

Guardiola C, Fleta C, Rodríguez J, Lozano M and Gómez F 2015c Preliminary microdosimetric measurements with ultra-thin 3D silicon detectors of a 62 MeV proton beam *J. Instrum.* **10** P01008

Guardiola C, Fleta C, Quirion D, Pellegrini G and Gómez F 2020 Silicon 3D microdetectors for microdosimetry in hadron therapy *Micromachines* **11** 1053

Gupta M *et al* 1991 The preparation, properties and applications of silicon nitride thin films deposited by plasma enhanced chemical vapour deposition *Thin Solid Films* **204** 77–106

Grün R, Friedrich T, Elsässer T, Krämer M, Zink K, Karger C P, Durante M, Engenhart-Cabillic R and Scholz M 2012 Impact of enhancements in the local effect model (LEM) on the predicted RBE-weighted target dose distribution in carbon ion therapy *Phys. Med. Biol.* **57** 7261–74

Hawkins R B 2003 A microdosimetric-kinetic model for the effect of non-Poisson distribution of lethal lesions on the variation of RBE with LET *Radiat. Res.* **160** 61–9

IAEA 2008 *Relative Biological Effectiveness in Ion Beam Therapy (TRS no 461)* (Vienna: International Atomic Energy Agency)

Int ICRU 1983 *Microdosimetry ICRU Report* 36 Bethesda, MD: ICRU

Kase Y, Kanai T, Matsufuji N, Furusawa Y, Elsasser T and Scholz M 2008 Biophysical calculation of cell survival probabilities using amorphous track structure models for heavy-ion irradiation *Phys. Med. Biol.* **53** 37–59

Kellerer A M 1985 Fundamentals of microdosimetry *The Dosimetry of Ionizing Radiation* ed K R Kase *et al* (New York: Academic) pp 78–158

Knoll G F 2010 Linear and logic pulse functions *Radiation Detection and Measurement* (New York: Wiley) ch 16, pp 584–646

Loncol T, Cosgrove V, Denis J M, Gueulette J, Mazal A, Menzel H G, Pihet P and Sabattier R 1994 Radiobiological effectiveness of radiation beams with broad LET spectra: microdosimetric analysis using biological weighting functions *Radiat. Prot. Dosim.* **52** 347–52

Magrin G 2018 A method to convert spectra from slab microdosimeters in therapeutic ion-beams to the spectra referring to microdosimeters of different shapes and material *Phys. Med. Biol.* **63** 215021

Niels Bassler O J, Christian Skou Søndergaard and Petersen J B 2010 Dose- and LET-painting with particle therapy *Acta Oncol.* **49** 1170–6

Niels Bassler J T, Lühr A, Singers Sørensen B, Scifoni E, Krämer M, Jäkel O, Saksø Mortensen L, Overgaard J and Petersen J B 2014 LET-painting increases tumour control probability in hypoxic tumours *Acta Oncol.* **53** 25–32

Paganetti H 2010 The physics of proton biology *Proton Therapy Physics* 1st edn (Boca Raton, FL: CRC Press) pp 593–626

Parker S, Kenney C J and Segal J 1997 3D-a proposed new architecture for solid-state radiation detectors *Nucl. Instrum. Methods Phys. Res.* A **395** 328–43

Prieto-Pena J, Gómez F, Fleta C, Guardiola C, Pellegrini G, Donetti M, Giordanengo S, González-Castaño D M and Pardo-Montero J 2019a Microdosimetric spectra measurements on a clinical carbon beam at nominal therapeutic fluence rate with silicon cylindrical microdosimeters *IEEE Trans. Nucl. Sci.* **66** 1840–7

Prieto-Pena J 2019b Development of silicon sensors for dosimetry and microdosimetry *PhD Thesis* Universidade de Santiago de Compostela http://hdl.handle.net/10347/20669

Prieto-Pena J, Gómez F, Guardiola C, Jimenez-Ramos M C, García-Lopez J, Baratto-Roldán A, Baselga M, Pardo-Montero J and Fleta C 2020 Impact of charge collection efficiency and electronic noise on the performance of solid state 3D-microdetectors *Phys. Med. Biol.* **65** 175004

Pellegrini G, Balbuena J, Bassignana D, Cabruja E, Fleta C, Guardiola C, Lozano M, Quirion D and Ullán M 2013 3D double sided detector fabrication at IMB-CNM *Nucl. Instrum. Methods Phys. Res.* A **699** 27–30

Rossi H H and Zaider M 1996 *Microdosimetry and its Applications* (Berlin: Springer)

Rosenfeld A B 2016 Novel detectors for silicon based microdosimetry, their concepts and applications *Nucl. Instrum. Methods Phys. Res.* A **809** 156–70

Schardt D, Elsässer T and Schulz-Ertner D 2010 Heavy-ion tumor therapy: physical and radiobiological benefits *Rev. Mod. Phys.* **82** 383–425

Sarrut D *et al* 2014 A review of the use and potential of the GATE Monte Carlo simulation code for radiation therapy and dosimetry applications *Med. Phys.* **41** 064301

Samnøy A T, Ytre-Hauge K S, Malinen E, Tran L, Rosenfeld A, Povoli M, Kok A, Summanwar A and Röhrich D 2020 Microdosimetry with a 3D silicon on insulator (SOI) detector in a low energy proton beamline *Radiat. Phys. Chem.* **176** 109078

Tran L T *et al* 2018 Thin silicon microdosimeter utilizing 3D MEMS fabrication technology: charge collection study and its application in mixed radiation fields *IEEE Trans. Nucl. Sci.* **65** 467–72

Zhang R, Taddei P J, Fitzek M M and Newhauser W D 2010 Water equivalent thickness values of materials used in beams of protons, helium, carbon and iron ions *Phys. Med. Biol.* **55** 2481–93

Ziegler J F, Ziegler M D and Biersack J P 2010 SRIM—the stopping and range of ions in matter (2010) *Nucl. Instrum. Methods Phys. Res.* B **268** 1818–23